

RSC Advances



This is an *Accepted Manuscript*, which has been through the Royal Society of Chemistry peer review process and has been accepted for publication.

Accepted Manuscripts are published online shortly after acceptance, before technical editing, formatting and proof reading. Using this free service, authors can make their results available to the community, in citable form, before we publish the edited article. This *Accepted Manuscript* will be replaced by the edited, formatted and paginated article as soon as this is available.

You can find more information about *Accepted Manuscripts* in the [Information for Authors](#).

Please note that technical editing may introduce minor changes to the text and/or graphics, which may alter content. The journal's standard [Terms & Conditions](#) and the [Ethical guidelines](#) still apply. In no event shall the Royal Society of Chemistry be held responsible for any errors or omissions in this *Accepted Manuscript* or any consequences arising from the use of any information it contains.

Observation of a magnetic phase transition but absence of electrical response in a new two-dimensional mixed-valence nickel-bis-dithiolene molecular crystal

Hao Yang,^a De-Yue An,^b Jian-Lan Liu,^a Xiao-Ming Ren,^{*a,c,d} Lan-Cheng Zhou,^a Hua-Bing Wang^{*b}

^a *State Key Laboratory of Materials-Oriented Chemical Engineering and College of Science, Nanjing Tech University, Nanjing 210009, People's Republic of China*

^b *Research Institute of Superconductor Electronics, Nanjing University, Nanjing 210093, People's Republic of China*

^c *College of Materials Science and Engineering, Nanjing Tech University, Nanjing 210009, People's Republic of China*

^d *State Key Laboratory & Coordination Chemistry Institute, Nanjing University, Nanjing 210093, People's Republic of China*

Phone: +86 25 58139476

Fax: +86 25 58139481

E-mail: xmren@njtech.edu.cn (XMR)

hbwang@nju.edu.cn (HBW)

Abstract

A new mixed-valence molecular crystal, $[\text{C}_3\text{-Apy}][\text{Ni}(\text{dmit})_2]_3$ (**1**) (dmit^{2-} = 2-thioxo-1,3-dithiole-4,5-dithiolate and $\text{C}_3\text{-Apy}^+$ = 4-amino-1-propylpyridinium) was synthesized utilizing a facile solution process and small size of counter-cation, this is distinct from the general strategy to obtain mixed-valence of $[\text{Ni}(\text{dmit})_2]$ molecular crystal that the large size counter-cation is desirable and the electrocrystallization method was used. The mixed-valence molecular crystal shows a magnetic phase transition around 77 K with a ca. 6 K thermal hysteresis loop. The crystal structure analysis at ambient temperature, the electronic band structure calculation based on the crystal structure, the variable temperature infrared spectra in 6-293 K and the conductance measurements in 4-295 K were further performed, the results revealed that **1** is a semiconductor and the magnetic phase transition is probably related to the electronic structure change in the $\{[\text{Ni}(\text{dmit})_2]_3\}^{1-}$.

Keywords: Nickel-bis-dithiolene complex, mixed-valence molecular crystal, magnetic transition, electronic band structure

1. Introduction

The planar $[M(\text{dmit})_2]$ ($\text{dmit}^{2-} = 2\text{-thioxo-1,3-dithiole-4,5-dithiolate}$; $M = \text{Ni, Pd}$ and Pt), an excellently building block, has been widely used to construct molecular crystals¹ with novel electrical,² photo-conducting³ or magnetic⁴ natures since 1960's.

The dithiolene unit in dmit^{2-} ligand extends with SR groups, this leads to the presence of versatile S...S interactions between neighboring $[\text{Ni}(\text{dmit})_2]$ moieties in crystal. The face-to-face π -stacking, lateral-to-lateral and head-to-tail intermolecular S...S contacts between the neighboring $[\text{Ni}(\text{dmit})_2]$ moieties could give rise to the molecular crystals with one-dimensional (1-D) chain,⁵ 1-D ladder,⁶ two-dimensional (2-D) layer,⁷ or three-dimensional (3-D) lattice⁸ of $[\text{Ni}(\text{dmit})_2]$.

The oxidation states of $[M(\text{dmit})_2]$ ($M = \text{Ni, Pd, Pt}$) span from -2 to 0, by contrast the molecular crystal with only $[M(\text{dmit})_2]^-$ species frequently obtained, the reports on mixed-valence $[M(\text{dmit})_2]$ molecular crystals are limited.⁹ To get mixed-valence $[M(\text{dmit})_2]$ ($M = \text{Ni, Pd, Pt}$) molecular crystal, the large size counter-cation is generally desirable¹⁰ and the electrocrystallization method is usually used.¹¹ These synthesis strategies produced the mixed-valence molecular crystals with various average oxidation states of $[M(\text{dmit})_2]^{n-}$, such as $n = 2/5$,^{11b} $2/3$,¹² $1/3$ ¹³ and $1/2$.¹⁴ In previous work, we got a mixed-valence $[\text{C}_8\text{-Apy}]_2[\text{Ni}(\text{dmit})_2]_3$ molecular crystal ($\text{C}_8\text{-Apy}^+ = 4\text{-amino-1-octylpyridinium}$) by inducing a small size $\text{C}_8\text{-Apy}^+$ into the $[M(\text{dmit})_2]$ lattice *via* the simple solution process. Interestingly, such a mixed-valence molecular crystal shows rapid, clear and stable response of photoconductivity under UV irradiation.¹⁵

In this paper, we report on a new mixed-valence molecular crystal, $[\text{C}_3\text{-Apy}][\text{Ni}(\text{dmit})_2]_3$ (**1**; $\text{C}_3\text{-Apy}^+ = 4\text{-amino-1-propylpyridinium}$), which shows a magnetic phase transition around 77 K with a *ca.* 6 K thermal hysteresis loop. We explored the possible origin of the phase transition *via* the investigation of variable temperature infrared spectra, temperature dependent conductivity, magnetic susceptibility and electronic band structure.

2. Experimental Section

2.1. Materials and chemicals

All chemicals and reagents were purchased from commercial sources and used without any further purification. 4, 5-di(thiobenzoyl)-1, 3-dithiole-2-thione was prepared according to the published procedure.¹⁶ [C₃-Apy]Br was synthesized using a similar procedure for preparation of [C₆-Apy]Br in the literature.¹⁷

2.2. Synthesis of [C₃-Apy][Ni(dmit)₂]₃

4, 5-di(thiobenzoyl)-1, 3-dithiole-2-thione (812 mg, 2 mmol) suspended in methanol (10 mL) was mixed with a methanol solution (10 mL) containing 184 mg (8 mmol) of sodium under argon atmosphere at ambient temperature. The mixture was stirred for 30 min to give a wine red solution. NiCl₂·6H₂O (238 mg, 1 mmol) and [C₃-Apy]Br (217 mg, 1 mmol) in methanol (20 mL) were added to the wine red solution with strongly stirring, and the precipitation was immediately formed. The solution of I₂ (127 mg, 0.5 mmol) and NaI (150 mg, 1 mmol) in methanol (20 mL) was then added to the above-obtained mixture with strongly stirring for 120 minutes. The microcrystalline product was collected by filtration, washed with MeOH and dried in vacuum. Yield: ~65%. Anal. Calc. for C₂₆H₁₃N₂S₃₀Ni₃ (**1**): C, 20.94; H, 0.88; N, 1.88%. Found: C, 21.16; H, 0.90; N, 1.89%. IR (KBr pellet, cm⁻¹): 1319, 1358 (ν_{C=C}), 1076, 1063 (ν_{C=S}), 507 and 503 (δ_{S-C-S}).

The dark green crystals of **1** suitable for X-ray diffraction analyses were obtained by slow evaporation of the solution of **1** in acetone at ambient temperature over 7-10 days. It is worth noting that we obtained the mixed-valence [Ni(dmit)₂] molecular crystal utilizing a facile solution process and small size of counter-cation, this is distinct from the general strategy that the large size counter-cation is desirable and the electrocrystallization method was used.

2.3. Physical Measurements

Elemental analyses (C, H and N) were performed on a Vario EL III elemental analyzer. Powder X-ray diffraction (PXRD) data were collected on a Bruker D8 Advance powder diffractometer with Cu Kα radiation (λ = 1.5418 Å). IR spectra were

recorded at room temperature on a Bruker VERTEX80V FTIR spectrometer (as KBr discs) under vacuum. Temperature-dependent FTIR spectra were recorded on a Thermo Nicolet 8700 spectrometer with a combination of an Oxford Variox AC-TL optical cryostat instrument. The sample temperature was controlled from 6 to 293 K through an ITC503 digital temperature controller. Magnetic susceptibility data were measured for polycrystalline samples on a Quantum Design MPMS-5S superconducting quantum interference device (SQUID) magnetometer, such a measurement was performed over the temperature range of 1.8-400 K in both cooling and warming modes. The measurement of variable temperature electrical conductivity based on four-probe method was made for two selected thin plate-shaped single crystals using a Keithley 2400 sourcemeter and Agilent 3440 1A digit multimeter, and the temperature varied between 4 and 295 K.

2.4. X-Ray single crystallography

Single-crystal X-ray diffraction data were collected on a Bruker Smart Apex II CCD detector with graphite-monochromated Mo K α radiation ($\lambda = 0.71073 \text{ \AA}$) at 296 K using the ω -scan technique. The data were integrated using the *SAINTE* program, which was also used for the intensity corrections for the Lorentz and polarization effects. An empirical absorption correction was applied using the *SADABS* program.¹⁸ The structure was solved by direct methods using the program *SHELXS-97* and all non-hydrogen atoms were anisotropically refined on F^2 by the full-matrix least-squares technique using the *SHELXL-97* crystallographic software package.¹⁹ All hydrogen atoms were placed at the calculated positions and refined as riding on the parent atoms. Details about data collection, structure refinement, and crystallography are summarized in Table 1.

2.5. Details of density functional theory calculation for electronic band structures and densities of states

Calculation for electronic band structure and densities of states (DOS) was performed using the CASTEP program²⁰ on the non-modelized crystal structure of **1**

which was obtained from X-ray single crystal structure analyses at room temperature. The electrons in the orbitals of Ni ($3d^84s^2$), S ($3s^23p^4$) and C ($2s^22p^2$) are treated as the valence electrons. The generalized gradient approximation (GGA) of Perdew-Burke-Ernzerhof (PBE)²¹ is used for the exchange-correlation functional. The k-points in the Brillouin zone were set to be $3\times 3\times 4$ according to the Monkhorst-Pack scheme.²² The plane wave basis set cut-off used is 270 eV and the convergence criterion is 2.0×10^{-6} eV/atom for all relevant calculations, and other calculating parameters were set to be the default values in the CASTEP code.

3. Results and discussion

3.1. Crystal structure

Compound **1** crystallizes in triclinic space group *P-1*. An asymmetric unit is comprised of one C_3 -APy⁺ cation together with three planar $[Ni(dmit)_2]$ units (ref. Figure 1). The bond lengths and angles in C_3 -APy⁺ cation fall within the expected values. All atoms are located in the general positions in the $[Ni(dmit)_2]$ moieties containing Ni(1), Ni(2) and Ni(3). The typical bond lengths in three different $[Ni(dmit)_2]$ species are summarized in Table 2. The total charge of three $[Ni(dmit)_2]$ moieties is 1⁻ since the cation shows 1⁺ charge, therefore, the averaged oxidation state of $[Ni(dmit)_2]$ moieties in an asymmetric unit is $-1/3$. For the $[Ni(dmit)_2]$ species, the bond C=C, Ni-S and C-S lengths are sensitive to its oxidation state. The theoretical analysis based on DFT calculations predicted that the lowest unoccupied molecule orbital (LUMO) of the neutral $[Ni(dmit)_2]^0$ consists of the 3d orbitals of Ni and the π orbital of ligand,¹⁵ and is bonding with respect to the $\pi(C=C)$ bond and antibonding with respect to the $\pi(C-S)$ and $\pi(Ni-S)$ bonds. The addition of one electron to the LUMO to give $[Ni(dmit)_2]^{1-}$ was expected to strengthen the $\pi(C=C)$ bond and weaken the $\pi(C-S)$, $\pi(Ni-S)$ bonds. As a result, the $\pi(C=C)$ bond distance is reduced, the $\pi(C-S)$ and $\pi(Ni-S)$ distances are increased with increasing n value in the series $[Ni(dmit)_2]^{n-}$ (n = 0, 1 and 2).^{11b} To inspect carefully the C=C, Ni-S and C-S lengths in **1**, it can be concluded that the $[Ni(dmit)_2]$ species containing Ni(2) and Ni(3) are neutral ones, while the $[Ni(dmit)_2]$ species containing Ni(1) has 1⁻ charge

(see Table 2). These assignments are further confirmed by theoretical analysis (Figure 6b-6d).

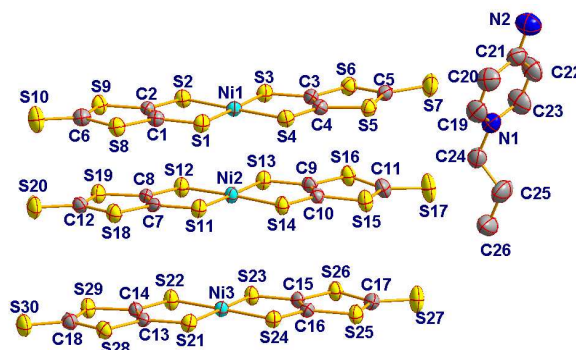


Figure 1 ORTEP view with non-hydrogen atom labeling and thermal ellipsoids at 30% probability level.

As displayed in Figure 2a, the C_3 -APy⁺ cations form monolayer molecular sheet, and the sheet is parallel to the crystallographic *ab*-plane. The pyridyl rings of the cations are parallel to each other owing to the restraint of inversion centers between them. The mixed-valence $[Ni(dmit)_2]$ species are stacked in a ...ABCABC... manner of ...Ni(2)Ni(1)Ni(3)... along *a*-axis direction, the neighboring $[Ni(dmit)_2]$ stacking columns are aligned along *b*-axis direction, to form a mixed-valence $[Ni(dmit)_2]$ layer. The cation layer (C) and mixed-valence $[Ni(dmit)_2]$ layer (M) are parallel to each other, and alternated in a fashion of ...MCMC... along *c*-axis. Within a $[Ni(dmit)_2]$ stack, the $[Ni(dmit)_2]$ species show face-to-face overlapping in the longitudinal offset mode; the dihedral angle and distance between the mean-molecular planes of $[Ni(dmit)_2]$ species, defined by four coordinated S atoms, is 1.30° and 3.517 Å between Ni(1)- and Ni(2)- $[Ni(dmit)_2]$ species, 1.31° and 3.482 Å between Ni(1)- and Ni(3)- $[Ni(dmit)_2]$ species, 0.82° and 3.625 Å between Ni(2)- and Ni(3)- $[Ni(dmit)_2]$ species; and as shown in Figure 2b, there exist the short interatomic contacts, which are less than the sum of van der Waals radii of two S atoms (3.7 Å), within and between the $[Ni(dmit)_2]$ stacks, and these typical interatomic distances are listed in Table 3, which indicate the existence of strongly intermolecular interactions in the

[Ni(dmit)₂] layer, while weak intermolecular interactions between the [Ni(dmit)₂] layers.

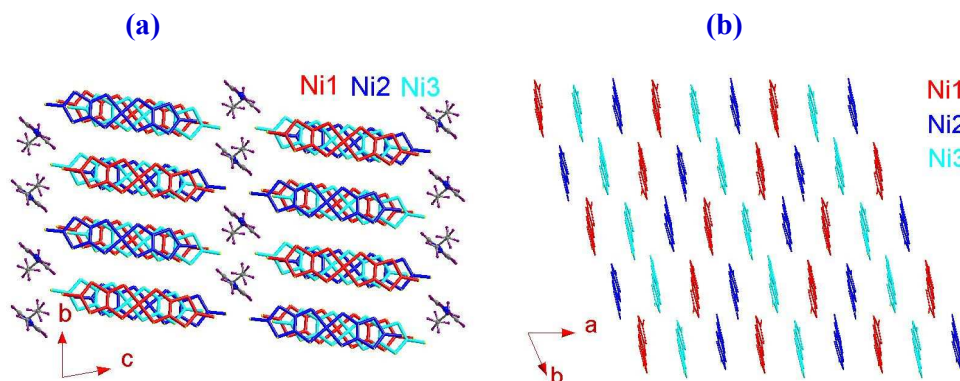


Figure 2 (a) Alternating layered packing structure viewed along the crystallographic *a*-axis direction in **1** (b) a monolayer of mixed-valence [Ni(dmit)₂] species and the different mixed-valence [Ni(dmit)₂] species are represented by different colors (Ni1: red; Ni2: blue and Ni3: cyan).

3.2. Magnetic property

Magnetic susceptibility (χ_m) of **1** as a function of temperature is displayed in Figure 3, in which χ_m represents the molar magnetic susceptibility with one [Ni(dmit)₂]¹⁻ species per formula unit. A magnetic phase transition appears around 77 K with a *ca.* 6 K hysteresis loop (insets in Figure 3) in the plot of χ_m versus T; above and below the transition temperature, molecular crystal **1** show Curie-Weiss magnetic behaviors, as a result, we firstly used Curie-Weiss law to estimate the average magnetic coupling interaction in crystal **1**. The experimental magnetic susceptibility data in high-temperature (HT) and low-temperature (LT) phases were fitted using Eq(1), respectively.

$$\chi_m = \frac{C}{T - \theta} + \chi_0 \quad (1)$$

where the χ_0 term represents the sum of the diamagnetic and possible van Vleck paramagnetic susceptibilities. The diamagnetism contributes from the atom cores and the van Vleck paramagnetism is related to the coupling of the ground and excited states through a magnetic field.²⁴ The best fit gave rise to the parameters $C = 0.360(3)$

$\text{emu}\cdot\text{K}\cdot\text{mol}^{-1}$, $\theta = -16.0(9)$ K and $\chi_0 = -6.2(1)\times 10^{-4}$ $\text{emu}\cdot\text{mol}^{-1}$ for the magnetic susceptibility data in the range of 96-400 K in HT phase; $C = 0.396(25)$ $\text{emu}\cdot\text{K}\cdot\text{mol}^{-1}$, $\theta = -9.0(5)$ K and $\chi_0 = -4.2(5)\times 10^{-3}$ $\text{emu}\cdot\text{mol}^{-1}$ for the magnetic susceptibility data in the range of 1.8-65 K in LT phase. Although the fitted C values in both HT and LT phases are close to the spin-only value (0.375 $\text{emu}\cdot\text{K}\cdot\text{mol}^{-1}$ when $g = 2.0$) for an $S = 1/2$ magnetic system, the fit yielded the diamagnetism χ_0 value in LT phase seems too larger. In addition to this, the antiferromagnetic (AFM) interaction is approximately proportional to the square of overlap integral of magnetic orbitals between the coupling magnetic centers,²⁵ and lattice shrinking in LT phase should lead to the overlap of magnetic orbitals being strengthened, namely, the AFM interaction should be stronger in LT phase than in HT phase. Thus, it is unreasonable that the Weiss constant, representing AFM interaction in the crystal **1**, in LT phase is less than that in HT phase.

For $[\text{Ni}(\text{dmit})_2]$ -based molecular crystals, the electronic and magnetic interactions between neighboring $[\text{Ni}(\text{dmit})_2]$ species are transmittable through long nonbonded interatomic contacts owing to the conjugated system in $[\text{Ni}(\text{dmit})_2]$ extending across the entire molecule. The crystal structural analysis demonstrated the existence of three types of contacts between neighboring $[\text{Ni}(\text{dmit})_2]$ species (1) the face-to-face stack within a $[\text{Ni}(\text{dmit})_2]$ column along a -axis direction, where the π -orbitals overlap is available (2) the lateral-to-lateral S...S contacts between the adjacent $[\text{Ni}(\text{dmit})_2]$ columns along b -axis direction and (3) the head-to-tail S...S contacts between the adjacent $[\text{Ni}(\text{dmit})_2]$ columns along the long molecular axis direction of $[\text{Ni}(\text{dmit})_2]$ (see Figure 2). Obviously, the magnetic coupling is stronger via the π -orbitals overlap than those via the lateral-to-lateral or head-to-tail S...S contacts. From this point, the analysis can be simplified as a 1-D spin system for the magnetic behavior of molecular crystal **1** in HT phase.

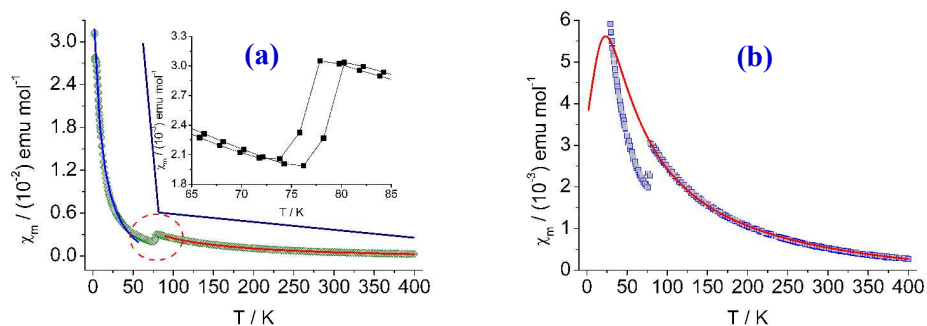


Figure 3 Temperature dependent χ_m of **1**. (a) The squares are the experimental data and the blue and red lines represent the fits using Curie-Weiss equation. The inset shows the thermal hysteresis loop. (b) The squares are the experimental data and the red line represents the fits for the magnetic susceptibility data in HT phase using 1-D uniform chain model.

In HT phase, the neighboring $S = 1/2$ $[\text{Ni}(\text{dmit})_2]^{1-}$ anions are separated by two neutral $[\text{Ni}(\text{dmit})_2]$ species (one $\text{Ni}(2)$ - $[\text{Ni}(\text{dmit})_2]$ and one $\text{Ni}(3)$ - $[\text{Ni}(\text{dmit})_2]$ species) within a stack (ref. Figure 2b), thus, a columnar $[\text{Ni}(\text{dmit})_2]$ stack can be thought as a $S = 1/2$ Heisenberg uniform linear chain. The magnetic susceptibility as a function of temperature for an $S = 1/2$ alternating chain system, derived from the spin Hamiltonian Eq.(2), is expressed as Eq.(3),

$$H = -2J \sum_{i=1}^{n/2} [\widehat{S}_{2i} \cdot \widehat{S}_{2i-1} + \alpha \widehat{S}_{2i} \cdot \widehat{S}_{2i+1}] \quad (2)$$

where J or αJ is the exchange integral between a spin and its right or left neighbor, respectively.

$$\chi_m(\text{chain}) = \frac{Ng^2 \mu_B^2}{k_B T} \cdot \frac{A + BX + CX^2}{1 + DX + EX^2 + FX^3} \quad (3)$$

In Eq.(3), A-F represent a set of parameters that depend on the alternating constant (α), $X = \mu/k_B T$ ($J < 0$ and $0 \leq \alpha \leq 1$). Extremely, when $\alpha = 0$ the alternating linear chain model is simplified to the dimer model with pairwise interactions and when $\alpha = 1$ the alternating linear chain model to the uniform linear-chain model.²⁶ If the diamagnetic and possible van Vleck paramagnetic susceptibilities are further

considered, the experimental molar magnetic susceptibility is given in the Eq. (4) form,

$$\chi_m = \chi_m(\text{chain}) + \chi_0 \quad (4)$$

The best fit was performed for the magnetic susceptibility data in the range of 96-400 K using Eq.(3) together with Eq.(4) to give $J/k_B = 17.5(2)$ K with $g = 2.0$ and $\chi_0 = -6.2(1) \times 10^{-4}$ emu·mol⁻¹ fixed or $J/k_B = 13.2(2)$ K, $g = 1.96(3)$ with $\chi_0 = -6.2(1) \times 10^{-4}$ emu·mol⁻¹ fixed. The theoretically reproduced χ_m - T plot is displayed in Figure 3b using the fitted parameters $J/k_B = 17.5(2)$ K, $g = 2.0$ and $\chi_0 = -6.2(1) \times 10^{-4}$ emu·mol⁻¹. The small J value indicated the existence of weakly AFM coupling within a [Ni(dmit)₂] stack in HT phase.

It is unavailable to further analyze the exact magnetic coupling nature in LT phase owing to lack of accessible crystal structure data.

3.3. Temperature dependent IR spectra

The temperature-dependent IR spectra of **1** in 6-293 K are shown in Figure S2, indicating that most of the vibrational bands show no sizable change in both intensity and the central position. The main alterations as the temperature changes concern the vibrational bands in four spectroscopy regions, which are respectively displayed in Figure 4a-4d. The band centered around 1319 cm⁻¹ and 1358 cm⁻¹ at 293 K are assigned to $\nu_{C=C}$ of the dmit²⁻ ligands; two bands are related to the neutral (1319 cm⁻¹) and negative (1358 cm⁻¹) [Ni(dmit)₂] species, respectively.²⁷ As the temperature drops, the band centered at 1319 cm⁻¹ shifts towards higher frequency, and a reflected point appeared at *ca.* 80 K if we connect sequentially the band maximum (Figure 4b) and this reflected point temperature is close to that the magnetic transition occurs; in addition to this, the shoulder around 1358 cm⁻¹ becomes a clear peak (see Figure 4a). The bands due to the $\nu_{C=S}$ mode of the dmit²⁻ ligands localize at 1063 cm⁻¹ and 1076 cm⁻¹ for [Ni(dmit)₂]⁻ at ambient temperature. As demonstrated in Figure 4c, the stretching vibration bands shift to higher frequency upon cooling.

The ν_{Ni-S} bands shift to high frequency in the [Ni(dithiolene)₂]ⁿ⁻ ($n = 0-2$) with the n value decreasing since the LUMO in the neutral [Ni(dithiolene)₂] species is

antibonding with respect to the $\sigma(\text{Ni-S})$ bonds. Nakamoto et al. theoretically analyzed the IR spectra of some $[\text{Ni}(\text{dithiolene})_2]^{n-}$, as indicated in Table 4, the change trend of $\nu_{\text{Ni-S}}$ band frequency with n value is in quite agreement with the observations.²⁸ As shown in Figure 4d, two weak bands centered at 485 and 455 cm^{-1} are observed at 293 K, which are probably originated from the Ni-S stretching vibrations in $[\text{Ni}(\text{dmit})_2]$ and $[\text{Ni}(\text{dmit})_2]^-$ species, respectively. The band around 485 cm^{-1} becomes weaker while the band around 455 cm^{-1} develops into visible and shifts towards high frequency upon cooling. Moreover, a reflected point also appeared at *ca.* 80 K if we connect sequentially the band maximum in low frequency side.

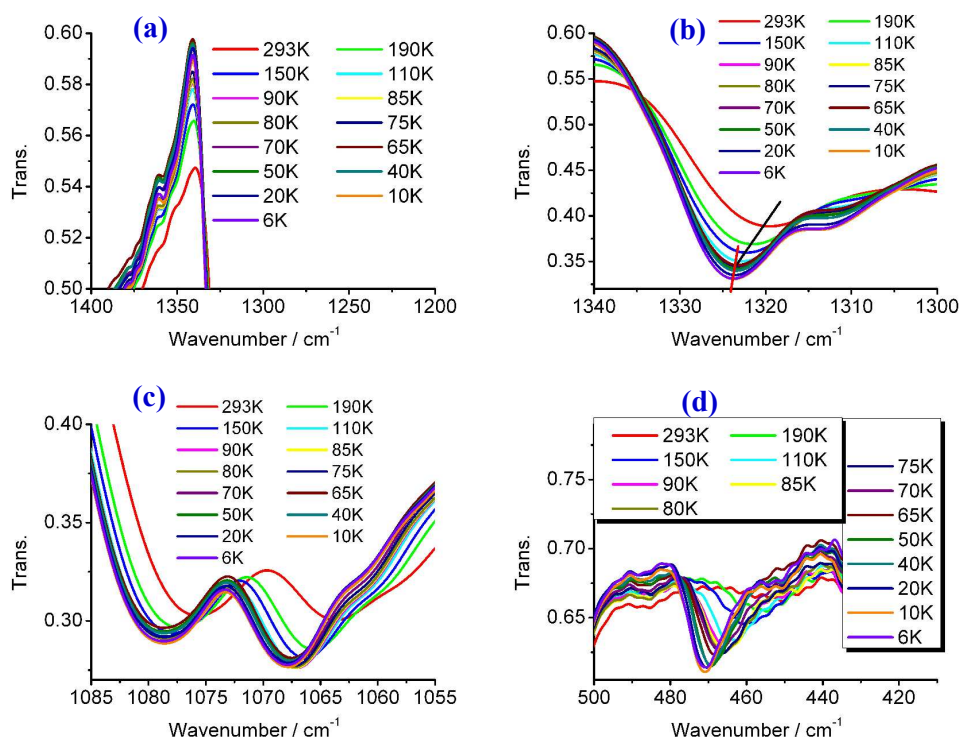


Figure 4 Variable-temperature IR spectra of **1** in the temperature range 6-293 K, showing changes in the shape and position of characteristic bands: a) and b) the $\nu_{\text{C=C}}$ bands of the dmit^{2-} ligands, c) the $\nu_{\text{C=S}}$ bands and d) the $\nu_{\text{Ni-S}}$ bands.

Vibrational band shifts indicate changes in the electronic state of molecule because the vibration frequency is directly related to the force constant of the bond. As mentioned above, the changes of bands from the intramolecular vibration modes ($\nu_{\text{C=C}}$, $\nu_{\text{C=S}}$ and $\nu_{\text{Ni-S}}$) within the $[\text{Ni}(\text{dmit})_2]$ and $[\text{Ni}(\text{dmit})_2]^-$ species indicate that

electron-vibration couplings within the mixed-valence $[\text{Ni}(\text{dmit})_2]$ species cooperate with the magnetic phase transition. In fact, it was known that the intramolecular vibrations played an important role in the occurrence of superconductivity of organic materials three decades ago, for which the molecular superconductivity was caused by electron-phonon interactions.^{29, 30} Upon cooling, the $\nu_{\text{C}=\text{C}}$ and $\nu_{\text{C}=\text{S}}$ bands shift to high frequency, representing the C=C and C=S bonds are strengthened in LT phase than those in HT phase; as well as the bands from $\nu_{\text{Ni-S}}$ of $[\text{Ni}(\text{dmit})_2]$ and $[\text{Ni}(\text{dmit})_2]^-$ species become invisible, and meanwhile a new band appears in their middle spectroscopy region, disclosing that the Ni-S bonds in $[\text{Ni}(\text{dmit})_2]^-$ species are strengthened in LT phase than those in HT phase, on the contrary, the Ni-S bonds in $[\text{Ni}(\text{dmit})_2]$ species are weakened in LT phase than those in HT phase. The above observation suggests that the electron localized in $[\text{Ni}(\text{dmit})_2]^-$ species in HT phase probably delocalizes between the neutral and negative $[\text{Ni}(\text{dmit})_2]$ species within a $[\text{Ni}(\text{dmit})_2]^0/[\text{Ni}(\text{dmit})_2]^{1-}/[\text{Ni}(\text{dmit})_2]^0$ unit in LT phase owing to the lattice shrinking in LT phase leading to more efficiently overlap of the frontier π -orbitals between $[\text{Ni}(\text{dmit})_2]$ and $[\text{Ni}(\text{dmit})_2]^-$ species. In previous study, we investigated the temperature dependent single crystal EPR spectra of 1-D molecular alloy $[\text{NO}_2\text{-BzPy}][\text{Ni}_x\text{Au}_{1-x}(\text{mnt})_2]$ systems, where $\text{NO}_2\text{-BzPy}^+$ is 4-nitrobenzyl-1-pyridinium, and we found the phenomenon that the electron delocalizes between the neighboring $[\text{Ni}(\text{mnt})_2]^-$ and $[\text{Au}(\text{mnt})_2]^-$ species within the $[\text{Ni}_x\text{Au}_{1-x}(\text{mnt})_2]^-$ columnar stack via the frontier π -orbitals overlap.³¹ Most recently, Stoddart and coworkers also discovered the electron delocalization in a rigid cofacial naphthalene-1, 8 : 4, 5-bis(dicarboximide) π -dimer via π - π stacking interaction.³²

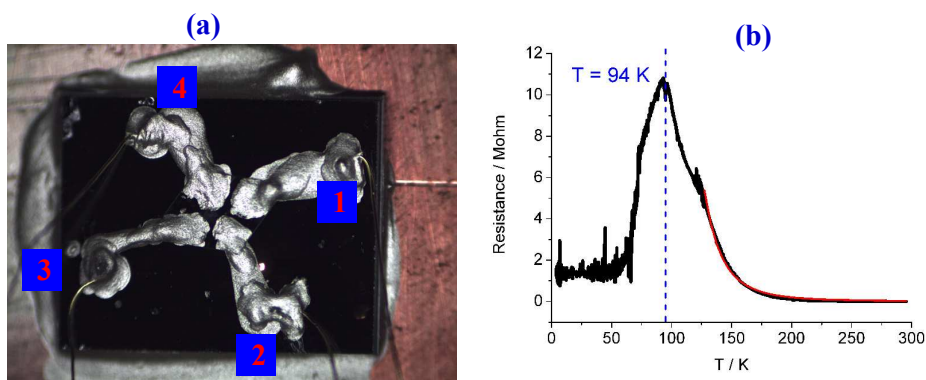
3.4. Conductivity

The thin plate-shaped single crystal was selected and the plate area is about $0.3 \times 0.4 \text{ mm}^2$, and as shown in Figure 5a, the four-probe method was used for the measurement of electrical conductivity. The resistance as a function of temperature is displayed in Figure 5b. Upon cooling, the resistance increases from ca. 2 kohm at 295 K to ca. 10 Mohms at 94 K, and then suddenly drops. The resistance abrupt decrease

below 94 K is due to that too high resistance of the crystal results in the current being under the instrument limitation. In order to investigate the conducting nature of molecular crystal **1** below 94 K, two 1 Mohms carbon film resistors were respectively connected in parallel between probes 1 and 2 as well as between probes 3 and 4 of the crystal (ref. Figure 5a), and the corresponding equivalent circuit is illustrated in Figure 5c. Extremely, in this case, the total resistance is zero when the crystal is a superconductor and the total resistance is 1 Mohms when the crystal is an insulator. The measured resistances against temperature are plotted in Figure 5d. It is worth noting that there is absence of anomaly around 77 K where a magnetic phase transition undergoes. On the other hand, we further fitted the temperature-dependent resistance in the range of 127-295 K to estimate the activation energy, E_a , using Arrhenius equation below,

$$R = R_0 \exp\left(\frac{E_a}{k_B T}\right) \quad (5)$$

In Eq.(5), R_0 , E_a and k_B correspond to the pre-exponential factor, activation energy and Boltzmann constant, respectively. The best fit gave $E_a = 1147.5(3)$ K (= 0.099eV) and the theoretically reproduced plot in the temperature range of 127-295 K is shown in Figure 5b.



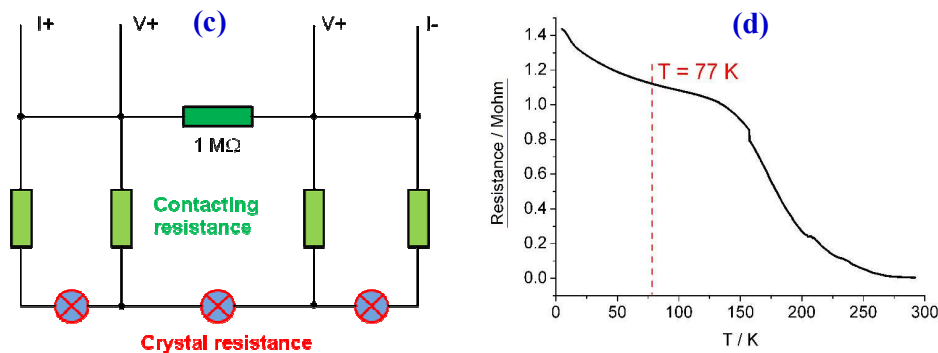


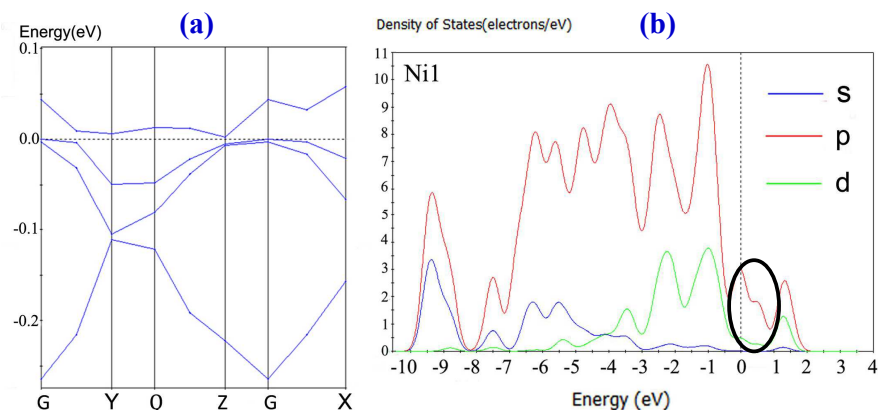
Figure 5 (a) Photograph of a thin plate-shaped single crystal with four-probes used in the variable temperature conductivity measurements. (b) Temperature dependence of the resistance of **1**, where the black line represents the measured data and the red line is fitted plot using Arrhenius equation in 127-295 K. (c, d) Illustration for the equivalent circuit when two 1 Mohms carbon film resistors were respectively connected in parallel between probes 1 and 2 as well as between probes 3 and 4 of the crystal and the corresponding plot of resistance against temperature.

3.5. Electronic band structure

The calculated bands near to the Fermi level along the high symmetry directions of the Brillouin zone are displayed in Figure 6a. By contrast, small dispersion is observed along the direction from G to Z in k-space, which is approximately parallel to the *c*-axis direction, this is indicative of weak orbital interactions between the mixed-valence $[\text{Ni}(\text{dmit})_2]$ layers and a 2-D electronic nature of this molecular crystal. The relatively sharp dispersion appears along the direction from G to Y and from G to X in k-space, indicating the existence of stronger orbital interactions within the mixed-valence $[\text{Ni}(\text{dmit})_2]$ layer. These results are in agreement to the crystal structure analysis that (1) the neighboring mixed-valence $[\text{Ni}(\text{dmit})_2]$ layers are separated by the cation layer and there exist shorter head-to-tail S...S contacts between inter-layers; (2) there exist strongly π - π stacking interactions within a mixed-valence $[\text{Ni}(\text{dmit})_2]$ column and much amounts of shorter lateral-to-lateral S...S contacts between the inter-columns in a mixed-valence $[\text{Ni}(\text{dmit})_2]$ layer. In addition, as displayed in Figure 6b-6d, the Partial DOS (PDOS) of the species with

Ni1 is different from other two $[\text{Ni}(\text{dmit})_2]$ species, whereas the PDOS of the species with Ni2 and Ni3 is quite analogous to each other near the Fermi level, representing that the electric state of Ni1 species is extremely different from those of Ni2 and Ni3 (the differences can be found in p-based band in Figure 6b-d) and further confirm that the $[\text{Ni}(\text{dmit})_2]$ species with Ni1 is monoanion and other two are neutral species, this finding is in good agreement with the analysis of crystal structure.

It was noted that the calculated energy gap between the highest occupied and the lowest unoccupied bands is 0.003 eV, however, this molecular crystal shows a semi-conductive behavior in the 4-295 K region. For this discrepancy between the theoretical and experimental results, it is understandable, because (i) it is well-known that the DFT method does not accurately describe the eigenvalues of the electronic states, causing the quantitative underestimation of band gaps;³³ (ii) for a system with a partially filled band, the normal metals and the magnetic insulator possess similar partially filled band when the calculated width of the partially filled band is narrow. In a so-called magnetic insulator, the effective on-site Coulomb repulsion energy (U_{eff}) is much larger than the hopping energy (t) that an electron transfers between two sites (the frontier orbitals between the neighboring molecules). However, the magnetic insulating state may become more stable than metallic state owing to electron-electron repulsion.³⁴ Both the analyses of crystal structural and PDOS revealed that the electron localizes in the $[\text{Ni}(\text{dmit})_2]^-$ species in HT phase, thus, molecular crystal **1** should be a magnetic insulator in HT phase.



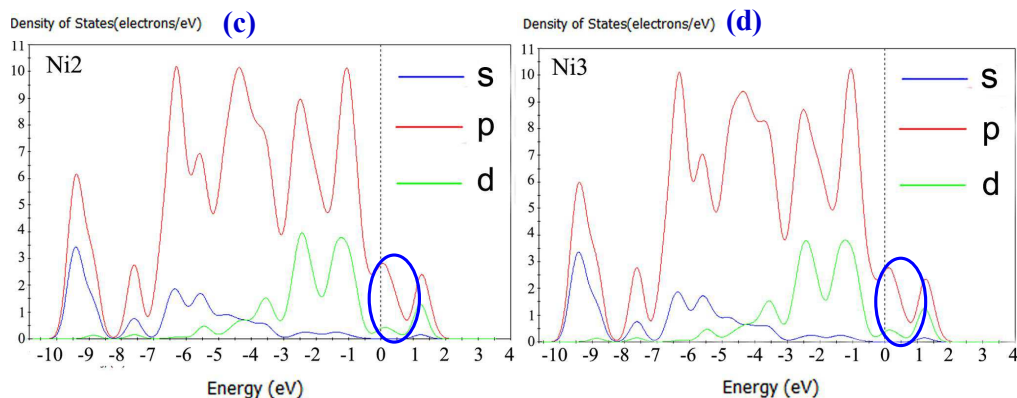


Figure 6 (a) Several highest occupied band and the lowest unoccupied bands in HT phase of **1**, where the Fermi levels are shown by dashed lines, k-points: G = (0, 0, 0), X = (0.5, 0, 0), Y = (0, 0.5, 0), Z = (0, 0, 0.5) and Q = (0, 0.5, 0.5) and (b-d) PDOS of three crystallographically different $[\text{Ni}(\text{dmit})_2]$ species.

4. Conclusion

In summary, we achieved a new mixed-valence molecular crystal $[\text{C}_3\text{-Apy}][\text{Ni}(\text{dmit})_2]_3$ using a facile solution process. The mixed-valence molecular crystal shows a hysteretic magnetic transition with *ca.* 6 K thermal hysteresis loop. The crystal structure and electronic band structure analyses revealed that the electron is localized in the $[\text{Ni}(\text{dmit})_2]^-$ monoanion in HT phase, and probably delocalized within $\dots[\text{Ni}(\text{dmit})_2]^0/[\text{Ni}(\text{dmit})_2]^{1-}/[\text{Ni}(\text{dmit})_2]^0\dots$ in LT phase owing to lattice shrinking, which leads to the frontier π -orbital overlap being strengthened within a $[\text{Ni}(\text{dmit})_2]^0/[\text{Ni}(\text{dmit})_2]^{1-}/[\text{Ni}(\text{dmit})_2]^0$ unit. The study on the variable temperature conductivity disclosed that this mixed-valence molecular crystal is a semiconductor.

Acknowledgment

Authors thank the Priority Academic Program Development of Jiangsu Higher Education Institutions and the National Nature Science Foundation of China (Grant nos.: 91122011 and 21271103) for financial support.

References

1. (a) R. Kato, *Chem. Rev.*, 2004, **104**, 5319; (b) P. Cassoux, L. Valade, H. Kobayashi, A. Kobayashi, R. A. Clark and A. E. Underhill, *Coord. Chem. Rev.*, 1991, **110**, 115. (c) T. Akutagawa and T. Nakamura, *Coord. Chem. Rev.*, 2000, **198**, 297; (d) A. Kobayashi, E. Fusjiwara and H. Kobayashi, *Chem. Rev.*, 2004, **104**, 5243.
2. (a) T. Nakamura, T. Akutagawa, K. Honda, A. E. Underhill, A. T. Coomber and R. H. Friend, *Nature*, 1998, **394**, 159; (b) T. Akutagawa, H. Koshinaka, D. Sato, S. Takeda, S.-I. Noro, H. Takahashi, R. Kumai, Y. Tokura and T. Nakamura, *Nat. Mater.*, 2009, **8**, 342.
3. (a) T. Naito, T. Karasudani, S. Mori, K. Ohara, K. Konishi, T. Takano, Y. Takahashi, T. Inabe, S. Nishihara and K. Inoue, *J. Am. Chem. Soc.*, 2012, **134**, 18656; (b) T. Ishikawa, N. Fukazawa, Y. Matsubara, R. Nakajima, K. Onda, Y. Okimoto, S. Koshihara, M. Lorenc, E. Collet, M. Tamura and R. Kato, *Phys. Rev. B*, 2009, **80**, 115108; (c) N. Fukazawa, T. Tanaka, T. Ishikawa, Y. Okimoto, S. Koshihara, T. Yamamoto, M. Tamura, R. Kato and K. Onda, *J. Phys. Chem. C*, 2013, **117**, 13187.
4. T. Kusamoto, H. M. Yamamoto, N. Tajima, Y. Oshima, S. Yamashita and R. Kato, *Inorg. Chem.*, 2013, **52**, 4759.
5. N. Takamatsu, T. Akutagawa, T. Hasegawa, T. Nakamura, T. Inabe, W. Fujita and K. Awaga, *Inorg. Chem.*, 2000, **39**, 870.
6. (a) T. Akutagawa, D. Sato, Q. Ye, T. Endo, S. I. Noro, S. Takeda and T. Nakamura, *Dalton Trans.*, 2010, **39**, 8219; (b) H. Imai, T. Otsuka, T. Naito, K. Awaga and T. Inabe, *J. Am. Chem. Soc.*, 1999, **121**, 8098.
7. Y. Kosaka, H. M. Yamamoto, A. Nakao, M. Tamura and R. Kato, *J. Am. Chem. Soc.*, 2007, **129**, 3054.
8. D. J. Reefman, J. P. Cornelissen, J. G. Haasnoot, R. A. G. de Graaf and J. Reedijk, *Inorg. Chem.*, 1990, **29**, 3933.
9. (a) K. Takahashi, H. B. Cui, Y. Okano, H. Kobayashi, Y. Einaga and O. Sato, *Inorg. Chem.*, 2006, **45**, 5739; (b) T. Akutagawa, D. Sato, H. Koshinaka, M.

- Aonuma, S. I. Noro, S. Takeda and T. Nakamura, *Inorg. Chem.*, 2008, **47**, 5951;
- (c) T. Akutagawa, K. Shitagami, S. Nishihara, S. Takeda, T. Hasegawa, T. Nakamura, Y. Hosokoshi, K. Inoue, S. Ikeuchi, Y. Miyazaki and K. Saito, *J. Am. Chem. Soc.*, 2005, **127**, 4397.
10. (a) A. E. Pullen, H. L. Lui, D. B. Tanner, K. A. Abboud and J. R. Reynolds, *J. Mater. Chem.*, 1997, **7**, 377; (b) T. Nakamura, A. E. Underhill, A. T. Coomber, R. H. Friend, H. Tajima, A. Kobayashi and H. Kobayashi, *Synth. Met.*, 1995, **70**, 1061; (c) Y. S. J. Veldhuizen, J. G. Haasnoot and J. Reedijk, *Synth. Met.*, 1997, **86**, 1827; (d) Y. S. J. Veldhuizen, W. J. J. Smeets, N. Veldman, A. L. Spek, C. Faulmann, P. Auban-Senzier, D. Jérôme, P. M. Paulus, J. G. Haasnoot and J. Reedijk, *Inorg. Chem.*, 1997, **36**, 4930.
11. (a) T. Akutagawa, T. Nakamura, T. Inabe and A. E. Underhill, *Thin Solid Films*, 1998, **331**, 264; (b) J. Lieffrig, O. Jeannin, P. Auban-Senzier and M. Fourmigué, *Inorg. Chem.*, 2012, **51**, 7144.
12. (a) A. Miyazaki, A. Izuoka and T. Sugawara, *Bull. Chem. Soc. Jpn.*, 1993, **66**, 2832; (b) M.-L. Doublet, E. Canadell, B. Garreau, J.-P. Legros, L. Brossard, P. Cassoux and J.-P. Pouget, *J. Phys.: Condens. Matter*, 1995, **7**, 4673.
13. (a) A. E. Pullen, H.-L. Liu, D. B. Tanner, K. A. Abboud and J. R. Reynolds, *J. Mater. Chem.*, 1997, **7**, 377; (b) Y. S. J. Veldhuizen, J. G. Haasnoot, J. Reedijk, *Synth. Met.*, 1997, **86**, 1827.
14. (a) B. Pomare`de, B. Garreau, I. Malfant, L. Valade, P. Cassoux, J.-P. Legros, A. Audouard, L. Brossard, J.-P. Ulmet, M.-L. Doublet and E. Canadell, *Inorg. Chem.*, 1994, **33**, 3401; (b) H. Kim, A. Kobayashi, Y. Sasaki, R. Kato and H. Kobayashi, *Chem. Lett.*, 1987, 1799.
15. H. Yang, J. L. Liu, L. C. Zhou and X. M. Ren, *Inorg. Chem. Front.*, 2014, **1**, 426.
16. G. Steimecke, H. J. Sieler, R. Kirmse and E. Hoyer, *Phosphorus Sulfur Relat. Elem.*, 1979, **7**, 49.
17. H. B. Duan, X. M. Ren, L. J. Shen, W. Q. Jin, Q. J. Meng, Z. F. Tian and S. M. Zhou, *Dalton Trans.*, 2011, **40**, 3622.

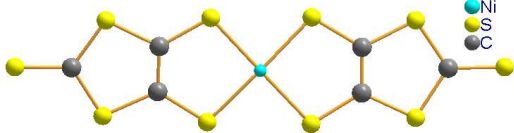
18. G. M. Sheldrick, *SADABS*, Program for Bruker Area Detector Absorption Correction, University of Göttingen, Göttingen, Germany, 1997.
19. G. M. Sheldrick, *SHELXS-97*, Program for Crystal Structure Solution, University of Göttingen, Göttingen, Germany, 1997.
20. (a) M. D. Segall, P. J. D. Lindan, M. J. Probert, C. J. Pickard, P. J. Hasnip, S. J. Clark and M. C. Payne, *J. Phys.: Condens. Matter*, 2002, **14**, 2717; (b) V. Milman, B. Winkler, J. A. White, C. J. Pickard, M. C. Payne, E. V. Akhmatkaya and R. H. Nobes, *Int. J. Quantum Chem.*, 2000, **77**, 895.
21. J. P. Perdew, K. Burke and M. Ernzerhof, *Phys. Rev. Lett.*, 1996, **77**, 3865.
22. H. J. Monkhorst and J. D. Pack, *Phys. Rev. B*, 1976, **13**, 5188.
23. (a) H. K. Fun, K. Sivakumar, J. L. Zuo, T. M. Yao and X. Z. You, *Acta Crystallogr. Sect. C: Cryst. Struct. Commun.*, 1996, **52**, 312; (b) M. J. J. Mulder, H. Kooijman, A. L. Spek, J. G. Haasnoot and J. Reedijk, *J. Chem. Cryst.*, 2002, **32**, 347; (c) J. P. Cornelissen, R. L. Loux, J. Jansen, J. G. Haasnoot, J. Reedijk, E. Horn, A. L. Spek, B. Pomarede, J. P. Legros and D. Reefman, *J. Chem. Soc., Dalton Trans.*, 1992, 2911; (d) N. Kushch, C. Faulmann, P. Cassoux, L. Valade, I. Malfant, J. P. Legros, C. Bowlas, A. Errami, A. Kobayashi and H. Kobayashi, *Mol. Cryst. Liq. Cryst. Sci. Technol. Sect. A*, 1996, **284**, 247.
24. J. H. van Vleck, *The Theory of Electric and Magnetic Susceptibilities*, Oxford, London, 1932.
25. M.-H. Whangbo, H.-J. Koo and D. Dai, *J. Solid State Chem.*, 2003, **176**, 417.
26. (a) J. Bonner and M. E. Fisher, *Phys. Rev. A.*, 1976, **235**, 640; (b) J. W. Hall, W. E. Marsh, R. R. Weller and W. E. Hatfield, *Inorg. Chem.*, 1981, **20**, 1033; (c) D. A. Tucker, P. S. White, K. L. Trojan, M. L. Kirk and W. E. Hatfield, *Inorg. Chem.*, 1991, **30**, 823.
27. (a) K. I. Pokhodnya, C. Faulmann, I. Malfant, R. Andreu-Solano, P. Cassoux, A. Mlayah, D. Smirnov and J. Leotin, *Synth. Met.*, 1999, **103**, 2016; (b) B. Cai, J. L. Liu, X. L. Sheng and X. M. Ren, *Inorg. Chem. Commun.*, **2011**, *14*, 1971; (c) M. K. Johnson, *Dithiolene chemistry: synthesis, properties, and applications*, *Prog. Inorg. Chem.*, Vol. 52, Chapter 4, John Wiley&Sons, USA, 2004.

28. C. W. Schl pfer and K. Nakamoto, *Inorg. Chem.*, 1975, **14**, 1338.
29. E. Demiralp, S. Dasgupta and W. A. Goddard, *J. Am. Chem. Soc.*, 1995, **117**, 8154.
30. T. Kato and T. Yamabe, *J. Chem. Phys.*, 2003, **119**, 5680.
31. X. M. Ren, Y. X. Sui, G. X. Liu and J. L. Xie, *J. Phys. Chem. A*, 2008, **112**, 8009.
32. Y. Wu, M. Frasconi, D. M. Gardner, P. R. McGonigal, S. T. Schneebeli, M. R. Wasielewski and J. F. Stoddart, *Angew. Chem. Int. Ed.*, 2014, **126**, 9630.
33. (a) R. W. Godby, M. Schluther and L. Sham, *J. Phys. Rev. B*, 1987, **36**, 6497; (b) C. M. I. Okoye, *J. Phys.: Condens. Matter*, 2003, **15**, 5945; (c) R. Terki, G. Bertrand and H. Aourag, *Microelectron. Eng.*, 2005, **81**, 514.
34. (a) M. H. Whangbo, J. M. Williams, P. C. W. Leung, M. A. Beno, T. J. Emge, H. H. Wang, K. D. Carlson and G. W. Crabtree, *J. Am. Chem. Soc.*, 1985, **107**, 581; (b) M. H. Whangbo and R. Hoffmann, *J. Am. Chem. Soc.*, 1978, **100**, 6093.

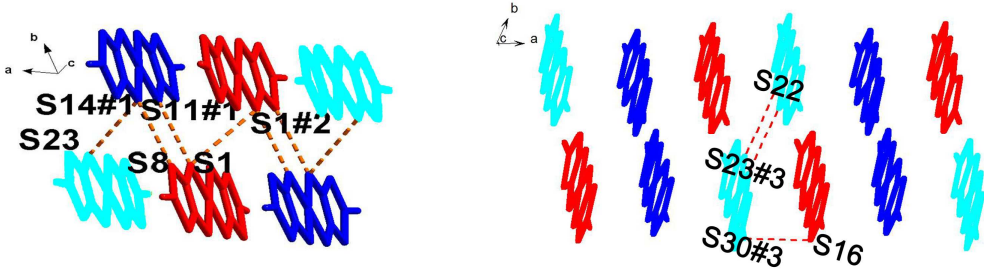
Table 1 Crystallographic data and refinement parameter for **1**

Temp. / K	296(2)
Wavelength / Å	0.71073
Formula	C ₂₆ H ₁₃ N ₂ Ni ₃ S ₃₀
Formula weight	1491.31
Space group	<i>P</i> -1
CCDC no.	1027558
Crystal system	Triclinic
<i>a</i> / Å	11.5235(13)
<i>b</i> / Å	12.6902(13)
<i>c</i> / Å	19.485(2)
<i>α</i> / °	74.904(3)°
<i>β</i> / °	75.852(4)°
<i>γ</i> / °	63.906(3)°
<i>V</i> / Å ³ , <i>Z</i>	2442.8(4)/2
<i>ρ</i> / g·cm ⁻¹	2.028
<i>μ</i> / mm ⁻¹	2.458
<i>F</i> (000)	1494.0
θ Range for data collection (°)	1.09 -27.55
	-14 ≤ <i>h</i> ≤ 14
Index ranges	-16 ≤ <i>k</i> ≤ 16
	-25 ≤ <i>l</i> ≤ 24
<i>R</i> _{int}	0.0912
Independent reflect. / restraints / parameters	11221/0/552
Refinement method	The least square refinement on <i>F</i> ²
Goodness-of-fit on <i>F</i> ²	1.008
<i>R</i> ₁ , <i>wR</i> ₂ ^a [<i>I</i> > 2σ(<i>I</i>)]	0.0646, 0.1209
<i>R</i> ₁ , <i>wR</i> ₂ ^a [all data]	0.1669, 0.1557
Residual / e·Å ⁻³	1.111/-0.647

$$^a R_1 = \sum ||F_o| - |F_c|| / |F_o|, \quad ^a wR_2 = [\sum w(\sum F_o^2 - F_c^2)^2 / \sum w(F_o^2)^2]^{1/2}.$$

Table 2 Average bond lengths in $[\text{Ni}(\text{dmit})_2]$ moiety of **1**


	Ni-S (Å)	S-C (Å)	C=C (Å)	Ref.
$[\text{Ni}(\text{dmit})_2]^{2-}$	2.195(9)	1.733(8)	1.352(3)	23a
$[\text{Ni}(\text{dmit})_2]^{1-}$	2.166(10)	1.715(10)	1.360(6)	23b
$[\text{Ni}(\text{dmit})_2]^{0.5-}$	2.163(3)	1.701(4)	1.382(7)	23c
$[\text{Ni}(\text{dmit})_2]^0$	2.143(3)	1.698(5)	1.393(10)	23d
Ni(1) moiety	2.165(13)	1.700(5)	1.375(6)	This work
Ni(2) moiety	2.154(13)	1.697(5)	1.384(6)	This work
Ni(3) moiety	2.152(13)	1.692(4)	1.384(6)	This work

Table 3 The typical short interatomic distances which are less than the sum of van der Waals radii of two S atoms (3.7 Å) in crystal of **1**


S(23)...S(14)#1	3.582 Å	S(3)...S(19)#1	3.597 Å
S(8)...S(14)#2	3.597 Å	S(16)...S(30)#3	3.540 Å
S(1)...S(11)#2	3.504 Å	S(27)...S(27)#4	3.536 Å
S(1)...S(1)#2	3.572 Å	S(17)...S(17)#5	3.313 Å

Symmetric codes: #1 = 1-x, 1-y, 1-z; #2 = 1-x, 1-y, 1-z; #3 = 1-x, 1-y, 1-z; #4 = -x, 1-y, 1-z; #5 = 1-x, -y, 1-z.

Table 4 Comparison of $\nu_{\text{Ni-S}}$ band frequencies (cm^{-1}) in bis(dithiolato)nickel²⁸

species	B _{2u}	B _{3u}	species	B _{2u}	B _{3u}
[Ni(S ₂ C ₂ H ₂) ₂] ⁰	428	398	[Ni(S ₂ C ₂ (CF ₃) ₂) ₂] ⁰	465	425
[Ni(S ₂ C ₂ H ₂) ₂] ⁻	411	385	[Ni(S ₂ C ₂ (CF ₃) ₂) ₂] ⁻	449	415
[Ni(S ₂ C ₂ (C ₆ H ₅) ₂) ₂] ⁰	475,408	454	[Ni(S ₂ C ₂ (CF ₃) ₂) ₂] ²⁻	422	394
[Ni(S ₂ C ₂ (C ₆ H ₅) ₂) ₂] ⁻	465,406	428	[Ni(S ₂ C ₂ (CN) ₂) ₂] ⁻	468,396	365
[Ni(S ₂ C ₂ (C ₆ H ₅) ₂) ₂] ²⁻	450,401	418	[Ni(S ₂ C ₂ (CN) ₂) ₂] ²⁻	457,365	357